Two Approaches to the Synthesis of Redox-Switchable 5,10,20-Triaryl-5,15-diazaporphyrinoids

Yui Murata,[b] Keisuke Sudoh,[b] Ko Furukawa,[c] Haruyuki Nakano,[d] and Yoshihiro Matano*[a]

Dedicated to Professor Atsuhiro Osuka on the occasion of his 70th birthday.

Despite the significant development and extensive application of phthalocyanine and related azaporphyrins, little attention has been paid to *meso-N*-substituted azaporphyrinoids. Here, we report new derivatives of 5,10,20-triaryl-5,15-diazaporphyrinoids (Ar$_3$DAP), which are reversibly redox-switchable between the 18π- and 19π-electron state. Four kinds of metal(II) complexes and free bases of Ar$_3$DAP were prepared by metal-templated cyclization of metal(II) complexes of 5,10,15-triaryl-10-azabiladiene-*ac* with sodium azide or copper-catalyzed *N*-phenylation of 10,20-diaryl-5,15-diazaporphyrins (Ar$_2$DAP) with diphenyliodonium hexafluorophosphate. In particular, regioselective *N*-phenylation of covalently linked Ar$_2$DAP dimer afforded two kinds of dimers bearing one or two *meso-N*-phenyl groups. Cyclic voltammetry revealed that attaching one aryl group onto the *meso*-nitrogen atom markedly changed the redox potentials of the DAP ring. The aromaticity and optical properties of the new Ar$_3$DAP π-electron systems were assessed using various spectroscopic measurements and density functional theory calculations. The distribution pattern of an electron spin in the neutral Ar$_2$DAP–Ar$_3$DAP radical revealed that the *meso*-N-phenyl group had a remarkable effect on spin delocalization of DAP π-radical. The present study provides valuable information for understanding the effects of the number of *meso-N*-substituents on azaporphyrin-based π-electron systems.

Introduction

Modifying the *meso*-methine units of porphyrin rings with nitrogen atoms changes molecular symmetry and energy levels of the highest occupied molecular orbital (HOMO) and lowest unoccupied molecular orbital (LUMO), with the changes depending on the number of *meso*-methine units modified.[1] Accordingly, this type of *meso*-modification is a promising and practical strategy to diversify the optical and redox properties of porphyrin π-electron systems while retaining their size and planarity. In addition to well-developed phthalocyanine (Pc) derivatives, azaporphyrins partially containing nitrogen at the *meso* position(s), such as 5-aza-, 5,15-diaza-, 5,10-diaza-, and 5,10,15-triaza-porphyrins, have long been studied from the perspectives of both fundamental and applied chemistry.[2] However, the number of partially *meso*-modified azaporphyrins

is still significantly lower than that of Pc derivatives, indicating that there is still room for developing *meso*-modification methods.

In 2016, we reported the first examples of 5,10,15,20-tetraaryl-5,15-diazaporphyrinoids (Ar$_4$DAP; **P1** in Scheme 1),[3] which were designed to markedly modify the HOMO and LUMO levels of 10,20-diaryl-5,15-diazaporphyrin[4] (Ar$_2$DAP) by attach-

5,10,15,20-Tetraaryl-5,15-diazaporphyrinoids (Ar$_4$DAP; **P1**)
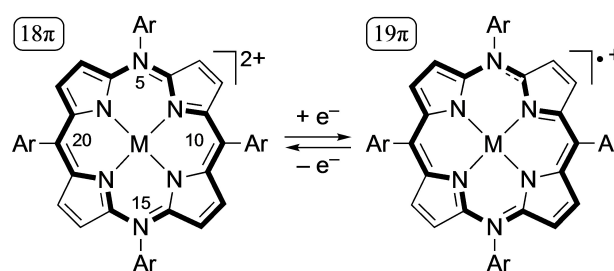
5,10,20-Triaryl-5,15-diazaporphyrinoids (Ar$_3$DAP; **This Work**)

Ar = aryl; M = Zn, Cu, Ni, Pt, 2H
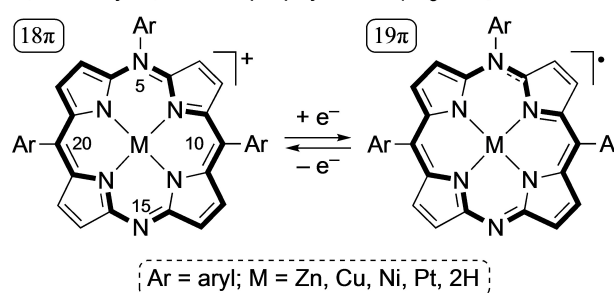
Scheme 1. Redox reactions of Ar$_4$DAP and Ar$_3$DAP derivatives.

[a] Y. Matano
Department of Chemistry, Faculty of Science, Niigata University, Nishi-ku, Niigata 950-2181, Japan
E-mail: matano@chem.sc.niigata-u.ac.jp

[b] Y. Murata, K. Sudoh
Department of Fundamental Sciences, Graduate School of Science and Technology, Niigata University, Nishi-ku, Niigata 950-2181, Japan

[c] K. Furukawa
Center for Coordination of Research Facilities, Institute for Research Administration, Niigata University, Nishi-ku, Niigata 950-2181, Japan

[d] H. Nakano
Department of Chemistry, Graduate School of Science, Kyushu University, Nishi-ku, Fukuoka 819–0395, Japan

Supporting information for this article is available on the WWW under https://doi.org/10.1002/asia.202401370

ing aryl groups to the two *meso*-nitrogen atoms. Owing to the two unshared electron pairs of the *meso*-nitrogen atoms in the DAP π-circuit, **P1** reversibly transforms among 20π, 19π, and 18π states via redox processes at potentials positively shifted from those of isoelectronic Ar$_2$DAP.[5] This redox property of **P1** indicates that its reduced oxidation states are remarkably air-stable, with both 19π-electron radical cation (Ar$_4$DAP·$^+$) and 20π-electron neutral antiaromatic compound (Ar$_4$DAP) isolated as air-stable solids. We investigated the properties of the new *meso*-N-arylated azaporphyrinoids **P1**, including their (anti)aromaticity,[6] electrical conductivity,[7] and non-innocent nature as the macrocyclic N$_4$ ligand.[8] To reveal the effect of the net charge on the optical and redox properties of the isoelectronic DAP ring, we also obtained the first examples of 5,10,20-triaryl-5,15-diazaporphyrinoids (Ar$_3$DAP in Scheme 1) as nickel(II) complexes (M = Ni).[9] The net charges of the DAP rings of Ar$_2$DAP, Ar$_3$DAP, and Ar$_4$DAP (**P1**) in the same 18π-electron oxidation state are 0, +1, and +2, respectively. Cyclic voltammetry (CV) of a series of the nickel(II) complexes of these DAP derivatives revealed that the redox potential derived from the 18π/19π redox couple of Ar$_3$DAP is more positive than that of Ar$_2$DAP but more negative than that of **P1**, with potential differences of 0.6–0.7 V. Furthermore, the neutral 19π-electron radical of the nickel(II) complex of Ar$_3$DAP was isolated and characterized. The clarified relationship between the number of *meso*-N-aryl groups and redox property enables the rational design of DAP-based functional dyes and catalysts, which are difficult to achieve using Ar$_2$DAP and **P1**. However, the previously reported method for preparing nickel(II) complexes of Ar$_3$DAP is not applicable to the synthesis of other metal complexes. Therefore, it is necessary to establish alternative methods to obtain various Ar$_3$DAP. Herein, we report two newly explored methods for the synthesis of several metal(II) complexes and free base of Ar$_3$DAP, in addition to their optical and redox properties. The number of N-phenyl groups was found to have significant effects on the fundamental properties of covalently linked Ar$_n$DAP–Ar$_n$DAP dimers (n = 2 and/or 3).

Results and Discussion

Synthesis

Scheme 2 depicts the new metal-templated method for the synthesis of zinc(II) and copper(II) complexes of 18π-electron Ar$_3$DAP cation (**2M**; M = Zn, Cu) from the corresponding metal(II) complexes of 5,10,15-triaryl-10-azabiladiene-*ac* (**1M-a**) and NaN$_3$. Compound **1Zn-a** was prepared from 1,9-dichloro-5-mesityldipyrrin (mesityl = 2,4,6-trimethylphenyl) in three steps using a reported procedure.[10] Heating a mixture of **1Zn-a** and NaN$_3$ in boiling N-methylpyrrolidone (NMP) for 20 min, followed by treatment with AgPF$_6$ at room temperature, afforded Zn^{II} complex **2Zn-a** as the pyridine (py) adduct in 5% yield, as confirmed with silica-gel column chromatography using CH$_2$Cl$_2$/acetone/pyridine as eluents (for details, see the Supporting Information; SI). When the reaction was conducted in boiling DMF, **2Zn-a** could not be obtained in acceptable yield. Trans-
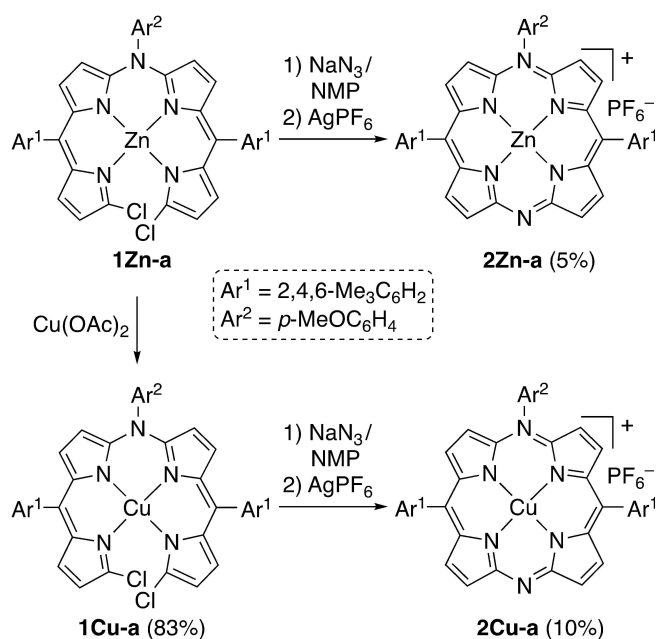
Scheme 2. Synthesis of **2M-a** (M = Zn, Cu). Ar^1 = Ar^2 = Ph for model **2Zn-m**.

metalation of **1Zn-a** with Cu(OAc)$_2$ occurred smoothly at room temperature to yield **1Cu-a**, which similarly underwent metal-templated cyclization with NaN$_3$ in NMP to afford Cu^{II} complex **2Cu-a** in 10% yield. Attempts to increase the yield of **2Zn-a** and **2Cu-a** by changing the reaction conditions failed owing to the inevitable formation of unidentified decomposition products.

Scheme 3 depicts the metal-templated synthesis of the lead(II) complex of Ar$_3$DAP cation (**2Pb-a**) and free base (**2H$_2$-a**).
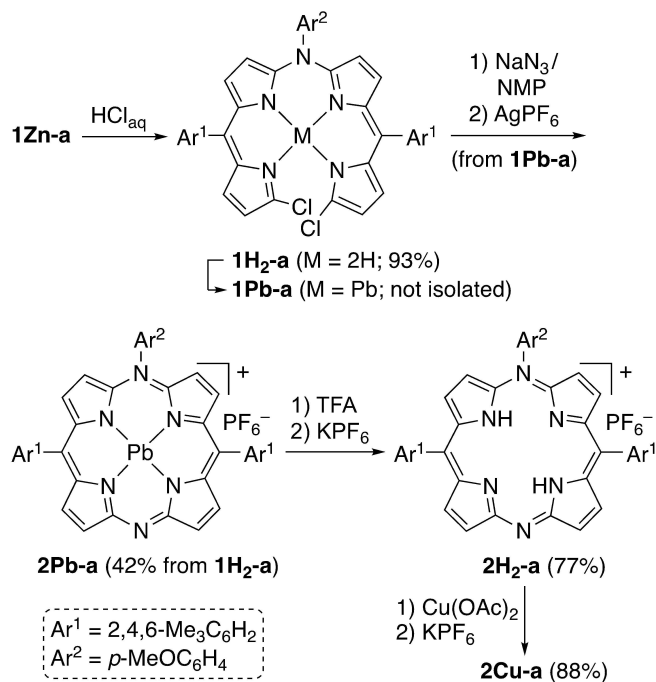
Scheme 3. Synthesis of **2M-a** (M = Pb, H$_2$, Cu).

Treatment of **1Zn-a** with aqueous HCl solution produced the free base of 5,10,15-triaryl-10-azabiladiene-*ac* **1H₂-a** in 93% yield. Complexation of **1H₂-a** with Pb(acac)₂ (acac=acetylacetonate) in NMP at room temperature generated lead(II) complex **1Pb-a**, as confirmed using mass spectrometry. Refluxing the resulting solution in the presence of NaN₃ for 20 min, followed by treatment of the cooled reaction mixture with AgPF₆, furnished Pb^{II} complex **2Pb-a** in 42% yield after silica-gel column chromatography. Demetalation of **2Pb-a** with trifluoroacetic acid (TFA) at room temperature and subsequent treatment with KPF₆ afforded **2H₂-a** in 77% yield. The efficiency of metal-templated cyclization of **1M-a** with NaN₃ strongly depends on the central metal. Thus, metalation of **2H₂-a** with Cu(OAc)₂ in CH₂Cl₂–MeOH proceeded rapidly at room temperature to produce **2Cu-a** in 88% yield after anion-exchange with KPF₆. The route shown in Scheme 3 provided **2Cu-a** from **1Zn-a** in superior overall yield (26%) compared with the route shown in Scheme 2.

Metal-templated cyclization of **1M** proved to be applicable to the synthesis of **2M**. However, the preparation of **1Zn-a**, the common precursor, requires a laborious separation process, and the overall yields of **2M** from 1,9-dichloro-5-mesityldipyrrin were unsatisfactory. Therefore, we developed an alternative synthetic route to **2M**, namely *meso-N*-phenylation of metal(II) complexes of Ar₂DAP (**3M**; M=Ni, Pt), as shown in Scheme 4.[11,12] The reaction conditions were based on Crivello's method for the synthesis of *N*-phenylacridine from acridine.[13] Heating a mixture of the nickel(II) complex of Ar₂DAP (**3Ni**), diphenyliodonium hexafluorophosphate (Ph₂IPF₆), and a catalytic amount of copper(II) benzoate (Cu(OBz)₂) in chlorobenzene at 120°C, followed by treatment with an aqueous KPF₆ solution at room temperature, afforded the nickel(II) complex of Ar₃DAP salt (**2Ni-b**) in 64% isolated yield under optimized conditions (for details, see Table S1 in SI). Only a trace amount of **2Ni-b** was obtained in the absence of Cu(OBz)₂, and the *meso-N*-phenylation did not proceed in DMF nor MeCN. Two other cupper(II) salts were also examined as catalysts: Cu(OAc)₂ was ineffective, and Cu(OSO₂CF₃)₂ did not catalyze this transformation (Table S1). Similarly, *N*-phenylation of the platinum(II) complex of Ar₂DAP (**3Pt**) produced Ar₃DAP salt **2Pt-b** in 34% yield. Notably, the newly developed *N*-phenylation method provided **2M** from 1,9-dibromo-5-mesityldipyrrin, the precursor of **3M**, in a few steps without the need for laborious separation
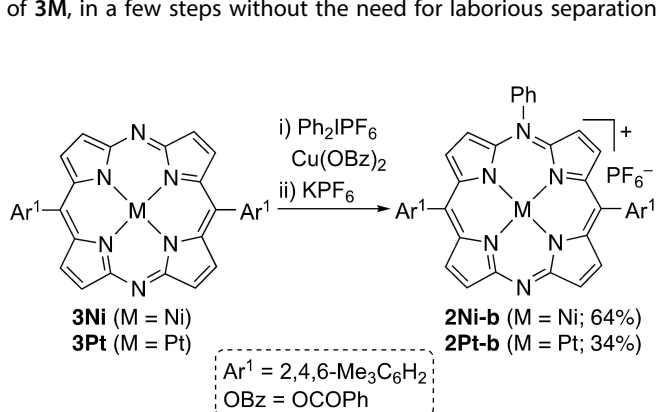
processes. Unfortunately, this method could not be directly applied to the synthesis of Zn^{II} complex **2Zn** and free base **2H₂**.

As shown in Scheme 5, treatment of 18π-electron Ar₃DAP salts **2M** with cobaltocene (CoCp₂) in THF at room temperature quantitatively produced the corresponding 19π-electron Ar₃DAP radicals **4M**, which were isolated as dark brown solids after recrystallization from CH₂Cl₂–MeOH. In solution, neutral radicals **4M** were slowly oxidized under air into cationic 18π-electron species (checked by UV/Vis/NIR absorption spectroscopy). The air stability of **4M** was appreciably lower than that of the isoelectronic cation radicals **P1**, reflecting the marked difference in their redox potentials owing to the 19π/18π redox couple (*vide infra*).

To demonstrate the synthetic advantage of *meso-N*-phenylation, covalently linked dimer Ar₂DAP–Ar₂DAP **5**[14] was used as the substrate to obtain *N*-phenylated derivatives Ar₂DAP–Ar₃DAP salt **6** and Ar₃DAP–Ar₃DAP salt **7** (Scheme 6). Treatment of **5** with Ph₂IPF₆ in the presence of Cu(OBz)₂ in refluxing chlorobenzene for 5 h afforded **6** and **7** in 38% and 20% yields, respectively, which were successfully separated from each other using silica-gel column chromatography. Notably, **6** and **7** are difficult to obtain using conventional metal-templated methods. Single-electron reduction of **6** with CoCp₂ produced Ar₂DAP–Ar₃DAP radical **8**, which was obtained as a dark brown solid (for details, see SI). A similar reduction of **7** with one equivalent of CoCp₂ generated radical cation **9**, although it could not be isolated in the pure form.[15]

Characterization and Aromaticity

Newly prepared Ar₃DAP derivatives **2M**, **4M**, **6**, **7**, and **8** were characterized using spectroscopic methods. In the high-resolution mass spectra, the fragment ion peaks [*M* − PF₆]⁺ were attributed to ionic compounds, and parent ion peaks [*M*]⁺ were ascribed to neutral radicals. The ¹H NMR spectra of **2M** (M=Zn, Ni, Pt, H₂) showed their pyrrolic-β proton (C$_\beta$—H) signals at 9.22–7.95 ppm, indicating that these protons were affected by the diatropic ring-current of the cationic DAP ring. Figure 1 depicts the ¹H NMR spectra of the three dimers, which exhibited

Scheme 4. Synthesis of **2M-b** from **3M** (M=Ni, Pt). Ar¹=Ph for model **2Pt-m**.
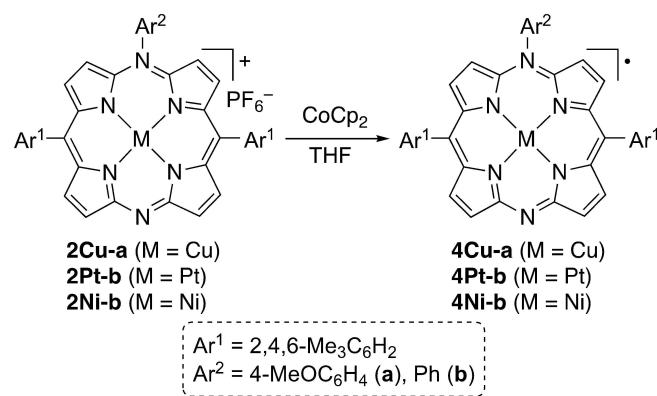
Scheme 5. Synthesis of **4M** from **2M**. The synthesis of **4Ni-b** from **2Ni-b** was previously reported in ref. [9]. Ar¹=Ar²=Ph for model **4Pt-m**.
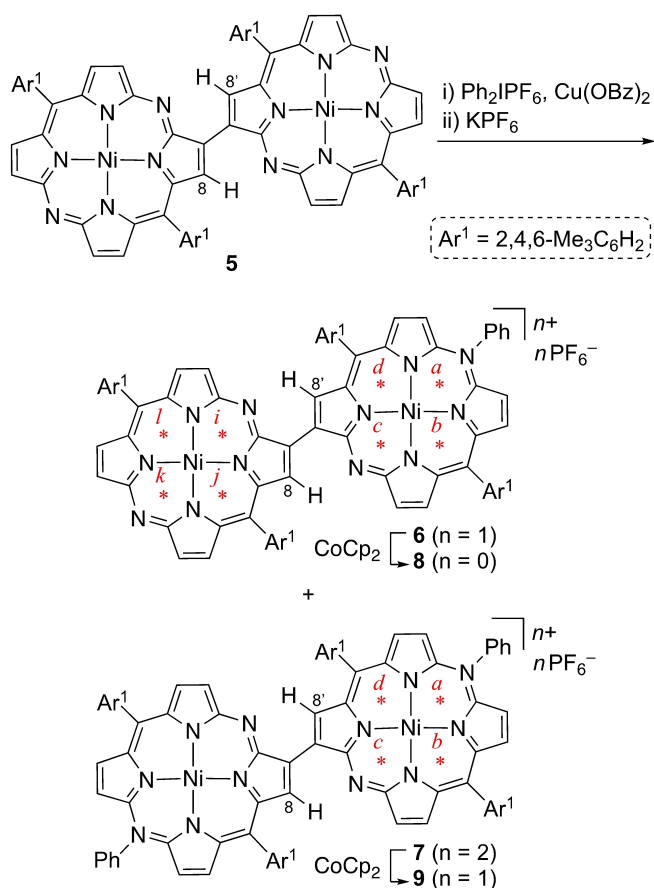
Scheme 6. Synthesis of **6–9**. $Ar^1 = Ph$ for dyad models **6-m** and **7-m**. NICS values at points *a–l* were calculated for **6-m** and **7-m**.
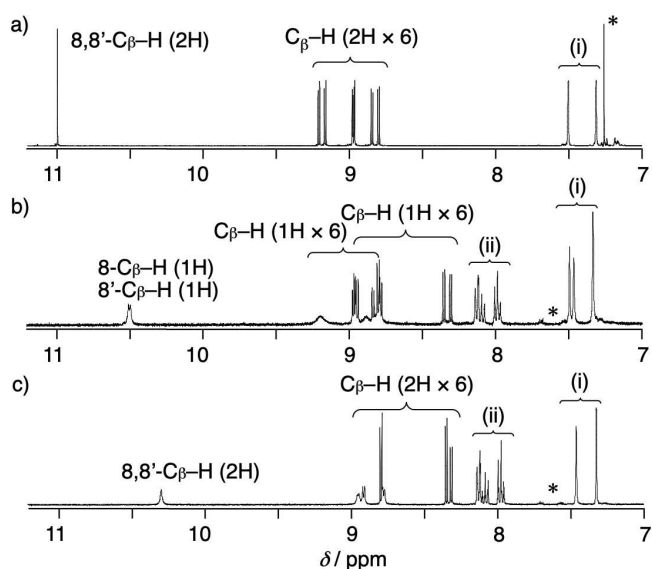

Figure 1. ^1H NMR spectra (11.2–7.0 ppm) of a) **5** in $CDCl_3$, b) **6** in CD_2Cl_2, and c) **7** in CD_2Cl_2. (i) *meta*-H signals of the mesityl groups. (ii) *N*-phenyl signals. Asterisks indicate residual solvent and plasticizer peaks.

different degrees of (i) diatropic ring-current effect derived from the DAP ring and (ii) intramolecular hydrogen bonding between C_β–H and *meso*-N atoms. As reported previously, **5** in $CDCl_3$

exhibits one set of C_β–H signals (2H×7) in the range of 11.0–8.79 ppm (Figure 1a). The ^1H NMR spectrum of **7** in CD_2Cl_2 (Figure 1c) showed one set of C_β–H signals (2H×7) attributed to the two symmetrical Ar_3DAP^+ rings at 10.29–8.31 ppm, which were upfield of the corresponding signals of **5**. These data suggested that the diatropic ring-current effect, namely aromatic character, of the Ar_3DAP^+ units in **7** was weaker than that of the Ar_2DAP units in **5**. Thus, adding a positive charge to the DAP ring reduces the total ring-current density, as inferred from our previous study on strapped Ar_4DAP derivatives.[6] The ^1H NMR spectrum of **6** displayed two sets of differently deshielded C_β–H signals (each, 1H×7), reflecting the different degrees of diatropic ring-current effects derived from the Ar_2DAP and Ar_3DAP^+ units. Thus, the two 18π-electron DAP rings in **6** have different degrees of aromaticity. Rotating-frame Overhauser effect spectroscopy was used to investigate the C_β–H signals attributed to the two different DAP units of **6**, revealing that the C_β–H signals of the neutral Ar_2DAP unit were overall more deshielded than those of the Ar_3DAP^+ unit. In the ^1H NMR spectra, the 8,8'-C_β–H signals were observed as singlets at 11.0 ppm (2H) for **5**, at 10.51 and 10.29 ppm (each, 1H) for **6**, and at 10.29 ppm (2H) for **7**. Deshielding of these 8,8'-C_β–H signals decreased in the order **5 > 6 > 7**, indicating that complementary intramolecular hydrogen bonding between C_β–H atoms adjacent to the inter-ring C–C bond and *meso*-N atoms weakened in the same order. Presumably, adding the positive charge to the DAP ring weakens the Lewis basicity of the lone electron pair of the *meso*-N atoms.

The experimentally observed results were corroborated by the nuclear-independent chemical shift (NICS),[16] calculated using Hartree-Fock method. The NICS(1) values at several positions of model compounds **6-m** and **7-m** (in Scheme 6), in which the mesityl groups were replaced by phenyl, are summarized in Table S2. The average NICS(1) values at positions *a–d* of the Ph_3DAP^+ ring in **6-m** (from −14.93 to −17.71 ppm) were close to those at the corresponding positions of the Ph_3DAP^+ ring in **7-m** (from −16.18 to −18.01 ppm) but less negative than those at positions *i–l* of the Ph_2DAP ring in **6-m** (from −18.52 to −19.44 ppm), indicating that the diatropic ring-current effect of the Ph_3DAP^+ unit was weaker than that of the isoelectronic Ph_2DAP unit. The relatively weaker aromaticity of Ph_3DAP^+ is attributable to its highly polarized structure,[17] which reduces the efficiency of the global π-electron delocalization in the DAP ring.

Optical and Redox Properties

The UV/Vis/NIR absorption spectra of the Ar_3DAP derivatives are shown in Figures 2 and S2, and their data are summarized in Table 1. The salts of 18π-electron Ar_3DAP **2M** (M = Ni,[9] Zn, Cu, Pt, H_2) exhibited intense absorption bands in the range of 500–700 nm (Figure 2a), whereas the neutral radicals of 19π-electron Ar_3DAP **4M** (M = Ni, Cu, Pt) exhibited intense NIR bands in the range of 730–830 nm (Figure 2b). The Q-like bands of **2M-a** (M = Zn, Cu; $\lambda_{max} = 628$ nm) were red-shifted from those of **3M** (M = Zn, Cu; $\lambda_{max} = 577–584$ nm)[4] but only slightly blue-shifted
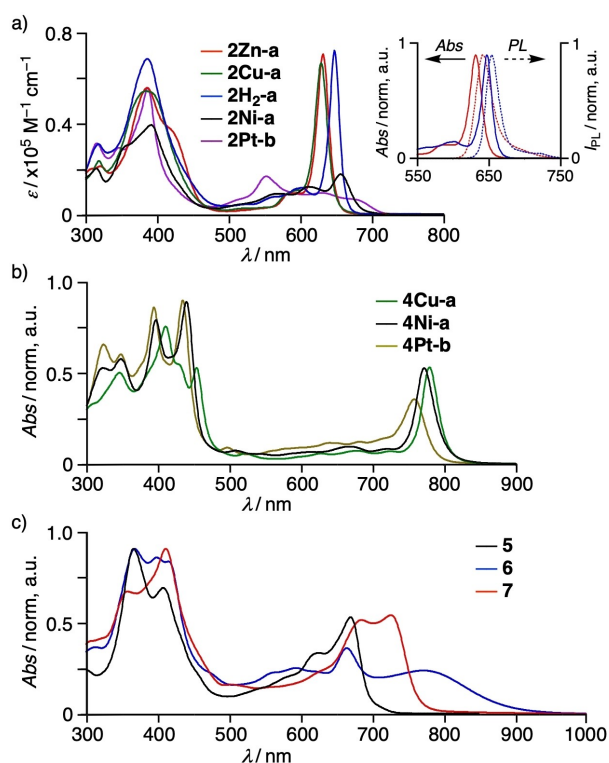
Figure 2. UV/Vis/NIR absorption spectra of a) **2M**, b) **4M**, and c) **5**, **6**, **7** in CH_2Cl_2. Absorption and fluorescence spectra of **2Zn-a** (red) and **2H$_2$-a** (blue) in CH_2Cl_2 are shown in the inset of a).

Table 1. Optical data for Ar$_3$DAP derivatives in CH_2Cl_2.[a]

DAP	λ_{max} [nm]
2Zn-a	386 (4.73), 628 (4.82)[b]
2Cu-a	383 (4.74), 628 (4.82)
2Ni-a[c]	391 (4.60), 568 (3.96), 611 (4.09), 655 (4.25)
2H$_2$-a	386 (4.83), 647 (4.86)[b]
2Ni-b[c]	392 (4.66), 566 (4.01), 612 (4.12), 657 (4.29)
2Pt-b	388 (4.73), 553 (4.22)
4Cu-a	411 (4.58), 454 (4.42), 780 (4.42)
4Pt-b	393 (4.65), 433 (4.70), 757 (4.27)
5[d]	365 (4.98), 406 (4.86), 669 (4.76)
6	368 (4.81), 400 (4.78), 416 (4.77), 594 (4.25), 665 (4.41), 773 (4.23)
7	411 (4.73), 686 (4.49), 727 (4.50)

[a] The absorption maxima ($\lambda_{max} > 360$ nm) are listed. [b] The fluorescence maxima (quantum yields) of **2Zn-a** and **2H$_2$-a** are 642 nm (0.073) and 654 nm (0.074), respectively. [c] Data from ref. [9]. [d] Data from ref. [14].

from those of **P1** (M = Zn, Cu; $\lambda_{max} = 631$–634 nm).[5] These data indicated that the optical HOMO–LUMO gaps of the 18π-electron Ar$_3$DAP$^+$ unit were smaller than that of the isoelectronic Ar$_2$DAP but larger than that of Ar$_4$DAP^{2+}. Time-dependent density functional theory (TD-DFT) calculations of model compounds allowed the assignment of the observed electronic transitions (Table S3).

The frontier orbitals of models of **2Zn-a** (**2Zn-m** in Scheme 2) and **2Pt-b** (**2Pt-m** in Scheme 4) are depicted in Figures S1 and S3, respectively. The HOMO, LUMO, and LUMO + 1 of **2Zn-m** were typical DAP π orbitals, whereas the HOMO − 1 and HOMO − 2 of **2Pt-m** comprised DAP-based p$_\pi$ orbitals mixed with Pt-centered d$_\pi$ orbitals. On the basis of the results of TD-DFT calculations, the longest absorption band of **2Zn-a** was assigned to pure HOMO-to-LUMO excitation, whereas the low-energy multiple absorption bands of **2Pt-b** were composed of HOMO-to-LUMO and HOMO − 2-to-LUMO excitations. Both **2Zn-a** and **2H$_2$-a** were fluorescent. In their fluorescence spectra (inset, Figure 2a), Stokes shifts were 350–160 cm^{-1}, reflecting the rigid π-framework of 18π-electron Ar$_3$DAP$^+$ dye.

The UV/Vis/NIR absorption spectra of covalently linked DAP dimers (dyads) **5**, **6**, and **7** are shown in Figure 2c. The longest absorption band of **7** ($\lambda_{max} = 727$ nm) was considerably red-shifted from that of **5** ($\lambda_{max} = 669$ nm), indicating that the optical HOMO–LUMO gap of the Ar$_3$DAP$^+$–Ar$_3$DAP$^+$ chromophore in **7** was smaller than that of the Ar$_2$DAP–Ar$_2$DAP chromophore in **5**. This was consistent with the difference in the HOMO–LUMO gaps of the corresponding monomers, **2Ni-b** and **3Ni**. In contrast, dyad **6** exhibited several broad absorption bands over the entire Vis/NIR region. The shape of this spectrum did not arise from a simple superposition of the spectra of the two components (monomers **2Ni-b** and **3Ni**). The spectral features of **6** and **7** were interpreted using DFT and TD-DFT calculations of their models, **6-m** and **7-m**. As shown in Figures 3 and 4, these dyads exhibited completely different orbital features. The HOMO and LUMO of **6-m** were mainly localized on the Ph$_2$DAP and Ph$_3$DAP$^+$ rings, respectively, reflecting the characteristics of each chromophore. In sharp contrast, both the HOMO and LUMO of **7-m** were efficiently delocalized over the two DAP rings. TD-DFT calculations revealed that the lowest excited state of **6-m**, formed mainly from the HOMO-to-LUMO electronic transition, had intramolecular charge-transfer (CT) character-istics. This was confirmed by the solvatochromic behavior of **6** (Figure S2d). The neutral radical **8** exhibited absorption bands at $\lambda_{max} = 600$ and 842 nm (Figure S2c), which were attributable to the π–π^* transitions of the Ar$_2$DAP and Ar$_3$DAP$^\bullet$ chromophores, respectively.

The redox potentials of the Ar$_3$DAP derivatives in CH_2Cl_2 were measured by CV and differential pulse voltammetry (DPV), with Bu$_4$NPF$_6$ as a supporting electrolyte. The results of monomers **2M** are summarized in Table 2 and Figure S4. In the observed range, **2M** exhibited two reversible redox processes, attributable to the 18π/19π and 19π/20π redox couples. The redox potentials (*E*) of **2Zn-a** were negatively shifted from those

Table 2. Redox potentials of Ar$_3$DAP **2M** in CH_2Cl_2 with Bu$_4$NPF$_6$.[a]

Ar$_3$DAP	*E* [V]	Ar$_3$DAP	*E* [V]
2Zn-a	−1.35, −0.73	2Ni-a[b]	−1.28, −0.63, + 1.17
2Cu-a	−1.29, −0.63, + 1.18	2Ni-b[b]	−1.23, −0.61, + 1.22
2H$_2$-a	−1.12, −0.43, + 1.37	2Pt-b	−1.21, −0.56, + 1.37

[a] Half-wave potentials (vs. ferrocene/ferrocenium; Fc/Fc$^+$) determined by CV unless otherwise noted. [b] Determined by DPV in this study.
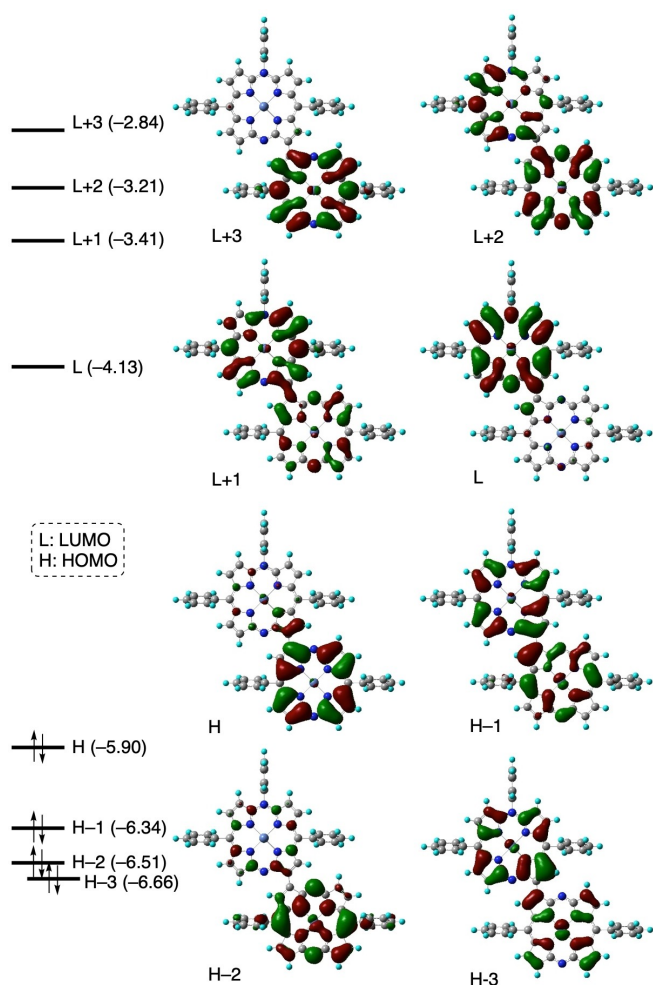
Figure 3. Selected Kohn-Sham orbitals and their energies (in eV) of **6-m** calculated by the DFT method with the solvent effect (PCM, CH₂Cl₂).
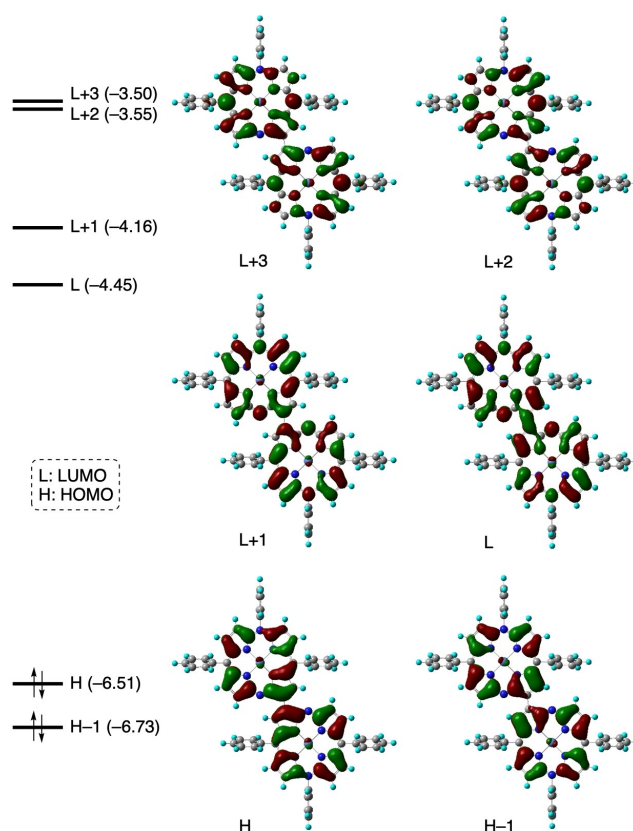

Figure 4. Selected Kohn-Sham orbitals and their energies (in eV) of **7-m** calculated by the DFT method with the solvent effect (PCM, CH₂Cl₂).

of **2Ni-a** and **2Cu-a**, reflecting the electronegativities of zinc (1.65, Pauling scale), nickel (1.91), and copper (1.90). The negatively shifted redox potential of **2Zn-a** indicated that the stability of its 19π-electron radical in air was low. The E of **2H₂-a** was more positive than those of the metal complexes. The same trend was observed for the E of the 18π/17π redox couple, which positively shifted in the order **2Ni-a**, **2Cu-a** < **2H₂-a**. Similarly, the redox potentials of **2Pt-b** were more positive than those of **2Ni-b** because the electronegativity of platinum (2.28) was larger than that of nickel. The electrochemical HOMO–LUMO gaps of **2M** determined using CV/DPV were in good agreement with the optical HOMO–LUMO gaps determined using UV/Vis absorption spectroscopy.

Figure 5 summarizes the results of CV and DPV of Ar₃DAP salt **2Ni-b**, Ar₂DAP **3Ni**, Ar₂DAP–Ar₃DAP salt **6**, and Ar₃DAP–Ar₃DAP salt **7**. Dyads **6** and **7** exhibited different electrochemical behaviors. In the observed range, **6** showed four reversible, one-electron redox processes. Compared with the electrochemical behavior of **2Ni-b** and **3Ni**, processes (ii) and (iii) corresponded to the 19π/20π and 18π/19π redox couples of the Ar₃DAP ring, respectively, whereas processes (i) and (iv) corresponded to the 18π/19π and 17π/18π redox couples of the
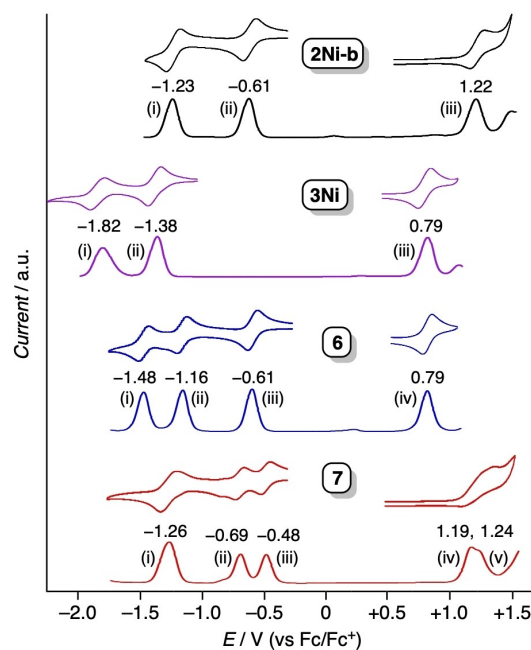

Figure 5. Cyclic voltammograms (upper) and differential pulse voltammograms (lower) of **2Ni-b** (black), **3Ni** (purple), **6** (blue), and **7** (red). Measured in CH₂Cl₂ with Bu₄NPF₆ as a supporting electrolyte. Scan rate = 60 mV s⁻¹ for CV. The peak potentials (vs. Fc/Fc⁺) determined by DPV are listed.

Ar$_2$DAP ring, respectively. The redox potentials for processes (i) (-1.48 V) and (ii) (-1.16 V) were negatively and positively shifted from the corresponding redox potentials of **3Ni** (-1.38 V) and **2Ni-b** (-1.23 V), respectively. These potential shifts were attributed to the electronic effects of the peripheral Ar$_3$DAP$^\bullet$ and Ar$_2$DAP substituents on the frontier orbitals of the adjacent DAP rings.

Dyad **7** showed three reversible and two quasi-reversible redox processes. Compared with the electrochemical behavior of **2Ni-b**, process (i) was likely one-step 20π/19π (2e$^-$) redox couple of the two Ar$_3$DAP rings, whereas processes (ii) and (iii) corresponded to the split 18π/19π (each, 1e$^-$) redox couple with a potential difference of approximately 0.2 V. This indicated that the electron spin was efficiently delocalized over the two DAP rings in the cation radical of **7**. Although isolation of **9** was unsuccessful, the singly occupied molecular orbital (SOMO) of **9-m** (Ar^1=Ph in Scheme 6) obtained using DFT calculations had a large orbital coefficient at the inter-ring C—C bond and the electron spin was spread over the entire molecule, supporting the experimental observation (Figure S5). Processes (iv) and (v) corresponded to the split 18π/17π (each, 1e$^-$) redox couple, but the potential difference was significantly smaller than that between (ii) and (iii), suggesting weaker stabilization of the trication radical.

To reveal the modes of electron-spin delocalization of Ar$_3$DAP radicals, electron paramagnetic resonance (EPR) spectra of CH$_2$Cl$_2$ solutions of **4Pt-b** and **8** were acquired at room temperature. As shown in Figure S6, **4Pt-b** exhibited an EPR signal at $g=1.9594$. Although hyperfine coupling was not clearly observed, DFT calculations of its model, **4Pt-m** (in Scheme 5), revealed that the unshared electron spin was delocalized over the DAP ring. As shown in Figure 6, dyad **8**
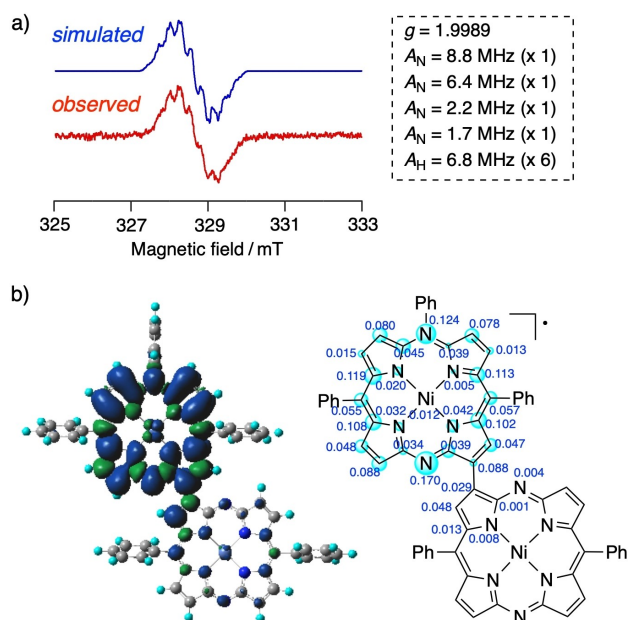
exhibited an EPR signal at $g=1.9989$, with the hyperfine structure derived from two meso-^{14}N, two core-^{14}N, and six C$_\beta$–^{1}H atoms. Notably, the electron spin was not distributed on the Ar$_2$DAP ring but mostly delocalized within the Ar$_3$DAP unit, as supported by DFT calculations of its model **8-m** (in Scheme 6). The SOMO had characteristics of the Ar$_3$DAP ring, albeit a highly coplanar configuration of two DAP rings (Figure S5). This is attributable to the large difference in orbital energies between the Ar$_3$DAP and Ar$_2$DAP rings.

Conclusions

We synthesized 18π- and 19π-electron Ar$_3$DAP derivatives and investigated their optical and electrochemical properties. Newly explored metal-templated cyclization and copper-catalyzed N-phenylation were used to synthesize the zinc(II), copper(II), nickel(II), and platinum(II) complexes and free base of Ar$_3$DAP. N-phenylation proved to be effective for regioselective meso-functionalization of covalently linked Ar$_2$DAP dimer, producing Ar$_3$DAP–Ar$_2$DAP and Ar$_3$DAP–Ar$_3$DAP dyads. The aromaticity and optical and electrochemical properties of Ar$_3$DAP derivatives were compared with those of the isoelectronic Ar$_2$DAP and Ar$_4$DAP derivatives. The diatropic ring-current effects of the 18π-electron Ar$_3$DAP cations were evaluated using NMR spectroscopy and NICS calculations, revealing that the aromaticity of the Ar$_3$DAP cations was relatively weak owing to their positively charged and polarized DAP π-electron systems. The redox potentials of the metal complexes of Ar$_3$DAP depended on the electronegativities of the central metals, resulting in the difference in air stability of the 19π-electron radicals. The low-energy UV/Vis/NIR absorption bands attributed to the π–π* transitions of the 18π- and 19π-electron Ar$_3$DAP chromophores appeared at 600–700 and 720–820 nm, respectively. Notably, the two kinds of dyads exhibited different optical and electrochemical properties. UV/Vis/NIR absorption spectroscopy and TD-DFT calculations revealed that the lowest excited states of Ar$_3$DAP–Ar$_2$DAP cation and Ar$_3$DAP–Ar$_3$DAP dication, formed mainly from their HOMO-to-LUMO electronic transitions, had charge-transfer and locally excited characteristics, respectively. The redox behaviors of these dyads also reflected their orbital characteristics. In the neutral radical of Ar$_3$DAP-Ar$_2$DAP, the electron spin was localized on the Ar$_3$DAP ring, reflecting a large difference in the orbital energies of the two DAP π-electron systems. In contrast, DFT calculations suggested that the electron spin in the cation radical of Ar$_3$DAP-Ar$_3$DAP dyad was delocalized over the two DAP rings owing to transannular interactions. Further development of novel azaporphyrinoids bearing meso-N-substituents is underway.

Figure 6. a) EPR spectra of **8** observed in CH$_2$Cl$_2$ and simulated. A: Hyperfine coupling constants. b) Spin density distribution at the optimized structure (left) and spin densities at the DAP ring (right) of **8-m**: calculated by the DFT method.

Experimental Section

General Remarks

All melting points were recorded on a micro melting point apparatus and are uncorrected. The NMR spectra were recorded on

400 MHz and 700 MHz (Agilent and Bruker) spectrometers. The ^1H and ^{13}C chemical shifts are reported in ppm as relative values vs. tetramethylsilane, and the ^{19}F and ^{31}P chemical shifts are reported in ppm as relative values vs. $CFCl_3$ and H_3PO_4, respectively. High-resolution mass (HRMS) spectra were measured on Thermo Fisher Scientific EXACTIVE (electron spray–quadrupole; ESI) and Bruker Autoflex III smartbeam (matrix assisted laser desorption/ionization–time of flight; MALDI-TOF) spectrometers. The UV/Vis/NIR absorption spectra were measured on JASCO V-530 and V-730 spectrometers, and the UV-Vis fluorescence spectra were measured on a JASCO EP-8300 spectrometer. Absolute fluorescence quantum yields were measured on a Hamamatsu Photonics Quantaurus-QY spectrometer. The IR (Attenuated Total Reflection; ATR or KBr) spectra were obtained on a JASCO FT/IR4600 spectrometer. Redox potentials and electrochemical behavior were measured at room temperature on an ALS model 650 E electrochemical workstation using a glassy carbon working electrode, a platinum wire counter electrode, and an Ag/Ag$^+$ [0.01 M AgNO$_3$, 0.1 M Bu$_4$NPF$_6$ (MeCN)] reference electrode. Thin-layer chromatography was performed with Kieselgel 60 F254, and preparative column chromatography was performed using Silica Gel 60 spherical, neutrality. All reactions were performed under an argon or nitrogen atmosphere unless otherwise noted. Compound **1Zn-a**[10] was prepared according to a reported procedure. Other chemicals and solvents were of reagent grade quality and used without further purification unless otherwise noted. For all the synthesis and characterization data of new compounds are reported in the Supporting Information.

DFT Calculations

The geometries of model compounds were optimized with the DFT method. The basis sets used for the optimization were the 6–311 G(d,p) basis set[18] for H, C, and N, the Wachters–Hay all electron basis set[19] supplemented with one f-function (exponent: 1.29 for Ni and 1.62 for Zn) for Ni and Zn, and the LANL2TZ(f) basis set (with effective core potentials)[20] for Pt. The functional of DFT was the Becke, three-parameter, Lee–Yang–Parr (B3LYP) exchange-correlation functional.[21] The optimized geometries were confirmed to be minima by vibrational analysis. The Cartesian coordinates and computed total energies of newly calculated models (**2Zn-m**, **4Pt-m**, **6-m**, **7-m**, **8-m**, and **9-m**) are summarized in Table S4. The excitation energies and oscillator strengths listed in Table S3 were computed with the TD-DFT method. The solvent effects were incorporated in both the DFT and TD-DFT calculations using the polarizable continuum model (PCM) with the integral equation formalism variant.[22] The NICS[23] values were calculated at the Hartree–Fock level with gauge-including atomic orbitals (GIAOs) at the DFT optimized geometries. The basis set used for the NICS calculations was 6–31 + G*.[24] All the calculations were carried out using the Gaussian 16 suite of programs.[25]

EPR Measurements

The EPR spectrum was measured at room temperature by using a JEOL JES-FA200 spectrometer equipped with an OXFORD ESR900 He-flow cryostat. A sample was prepared as a 0.1 mM solution in CH_2Cl_2. After three freeze-pump-thaw cycles, the solution sample in a quartz tube was sealed by frame. Spectral simulation was performed using EasySpin,[26] which is a MATLAB toolbox meant for this. The static magnetic field and microwave frequency were measured by an Echo Electronics EFM-2000 gauss meter and a TakedaRiken TR5212 microwave counter, respectively.

Conflict of Interests

The authors declare no conflict of interest.

Data Availability Statement

The data that support the findings of this study are available in the supplementary material of this article.

[1] a) K. Ishii, N. Kobayashi, in *The Porphyrin Handbook* Vol 16 (Eds.: K. M. Kadish, K. M. Smith, R. Guilard), Academic Press, San Diego, **2003**, pp. 1–42; b) H. Ogata, T. Fukuda, K. Nakai, Y. Fujimura, S. Neya, P. A. Stuzhin, N. Kobayashi, *Eur. J. Inorg. Chem.* **2004**, *2004*, 1621–1629.

[2] a) J. Mack, N. Kobayashi, *Chem. Rev.* **2011**, *111*, 281–321; b) Y. Matano, *Chem. Rev.* **2017**, *117*, 3138–3191; c) Y. Matano, *Org. Biomol. Chem.* **2023**, *21*, 3034–3056.

[3] T. Satoh, M. Minoura, H. Nakano, K. Furukawa, Y. Matano, *Angew. Chem. Int. Ed.* **2016**, *55*, 2235–2238.

[4] a) M. Horie, Y. Hayashi, S. Yamaguchi, H. Shinokubo, *Chem. Eur. J.* **2012**, *18*, 5919–5923; b) Y. Matano, T. Shibano, H. Nakano, H. Imahori, *Chem. Eur. J.* **2012**, *18*, 6208–6216; c) Y. Matano, T. Shibano, H. Nakano, Y. Kimura, H. Imahori, *Inorg. Chem.* **2012**, *51*, 12879–12890.

[5] a) K. Sudoh, T. Satoh, T. Amaya, K. Furukawa, M. Minoura, H. Nakano, Y. Matano, *Chem. Eur. J.* **2017**, *23*, 16364–16373; b) Y. Shimizu, Y. Matano, *J. Porphyrins Phthalocyanines* **2021**, *25*, 1004–1014; c) Y. Shimizu, Y. Matano, *J. Porphyrins Phthalocyanines* **2023**, *27*, 172–183.

[6] H. Ochiai, K. Furukawa, H. Nakano, Y. Matano, *J. Org. Chem.* **2021**, *86*, 2283–2296.

[7] Y. Satoh, Y. Fujita, N. Muramatsu, K. Furukawa, T. Ikoma, M. Minoura, H. Nakano, Y. Matano, *ChemPlusChem* **2021**, *86*, 1476–1486.

[8] Y. Satoh, Y. Kudoh, K. Furukawa, Y. Matano, *Org. Lett.* **2022**, *24*, 3839–3843.

[9] K. Sudoh, T. Hatakeyama, K. Furukawa, H. Nakano, Y. Matano, *J. Porphyrins Phthalocyanines* **2018**, *22*, 542–551.

[10] K. Sudoh, K. Furukawa, H. Nakano, S. Shimizu, Y. Matano, *Heteroatom Chem.* **2018**, *29*, e21456.

[11] The *N*-methylation of **3M** with methyl triflate was reported by Shinokubo et al. a) W. X. Chia, M. Nishijo, S. Kang, J. Oh, T. Nishimura, H. Omori, J.-F. Longevial, Y. Miyake, D. Kim, H. Shinokubo, *Chem. Eur. J.* **2020**, *26*, 2754–2760; b) M. Nishijo, S. Mori, T. Nishimura, H. Shinokubo, Y. Miyake, *Chem. Asian J.* **2022**, *17*, e202200305.

[12] The N-alkynylation of a 5,10,15,20-tetraazaporphyrin with a hypervalent iodine(III) reagent was reported by Uchiyama et al. N. Toriumi, N. Asano, K. Miyamoto, A. Muranaka, M. Uchiyama, *J. Am. Chem. Soc.* **2018**, *140*, 3858–3862.

[13] J. V. Crivello, J. L. Lee, *J. Polym. Sci., Part A: Polym. Chem.* **2014**, *48*, 4484–4495.

[14] Y. Matano, D. Fujii, T. Shibano, K. Furukawa, T. Higashino, H. Nakano, H. Imahori, *Chem. Eur. J.* **2014**, *20*, 3342–3349.

[15] UV/Vis/NIR spectroscopy suggested the generation of **9** in solution (λ_{max} = 1058 nm in CH_2Cl_2). However, attempts to isolate **9** by recrystallization or column chromatography were unsuccessful because it was gradually oxidized to **7** under ambient conditions.

[16] a) P. V. R. Schleyer, C. Maerker, A. Dransfeld, H. Jiao, N. J. R. van Eikema Hommes, *J. Am. Chem. Soc.* **1996**, *118*, 6317–6318; b) Z. Chen, C. S. Wannere, C. Corminboeuf, R. Puchta, P. V. R. Schleyer, *Chem. Rev.* **2005**, *105*, 3842–3888.

[17] The dipole moments calculated by the DFT method were 7.44 D for the Ni^{II} complex of Ph$_3$DAP$^+$ and 27.09 D for **6-m**.

[18] R. Krishnan, J. S. Binkley, R. Seeger, J. A. Pople, *J. Chem. Phys.* **1980**, *72*, 650–654.

[19] a) A. J. H. Wachters, *J. Chem. Phys.* **1970**, *52*, 1033–1036; b) P. J. Hay, *J. Chem. Phys.* **1977**, *66*, 4377–4384; c) K. Raghavachari, G. W. Trucks, *J. Chem. Phys.* **1989**, *91*, 1062–1065.

[20] a) P. J. Hay, W. R. Wadt, *J. Chem. Phys.* **1985**, *82*, 299–310; b) L. E. Roy, P. J. Hay, R. L. Martin, *J. Chem. Theory Comput.* **2008**, *4*, 1029–1031; c) A. W. Ehlers, M. Böhme, S. Dapprich, A. Gobbi, A. Höllwarth, V. Jonas, K. F. Köhler, R. Stegmann, A. Veldkamp, G. Frenking, *Chem. Phys. Lett.* **1993**, *208*, 111–114.

[21] a) A. D. Becke, *J. Chem. Phys.* **1993**, *98*, 5648–5652; b) C. Lee, W. Yang, R. G. Parr, *Phys. Rev. B* **1988**, *37*, 785–789.

[22] E. Cancès, B. Mennucci, J. Tomasi, *J. Chem. Phys.* **1997**, *107*, 3032–3041.

[23] P. V. R. Schleyer, C. Maerker, A. Dransfeld, H. Jiao, N. J. R. van Eikema Hommes, *J. Am. Chem. Soc* **1996**, *118*, 6317–6318.

[24] a) W. J. Hehre, R. Ditchfield, J. A. Pople, *J. Chem. Phys.* **1972**, *56*, 2257–2261; b) P. C. Hariharan, J. A. Pople, *Theor. Chim. Acta* **1973**, *28*, 213–222; c) T. Clark, J. Chandrasekhar, G. W. Spitznagel, P. V. R. Schleyer, *J. Comput. Chem.* **1983**, *4*, 294–301; d) V. A. Rassolov, J. A. Pople, M. A. Ratner, T. L. Windus, *J. Chem. Phys.* **1998**, *109*, 1223–1229.

[25] M. J. Frisch, G. W. Trucks, H. B. Schlegel, G. E. Scuseria, M. A. Robb, J. R. Cheeseman, G. Scalmani, V. Barone, G. A. Petersson, H. Nakatsuji, X. Li, M. Caricato, A. V. Marenich, J. Bloino, B. G. Janesko, R. Gomperts, B. Mennucci, H. P. Hratchian, J. V. Ortiz, A. F. Izmaylov, J. L. Sonnenberg, D. Williams-Young, F. Ding, F. Lipparini, F. Egidi, J. Goings, B. Peng, A. Petrone, T. Henderson, D. Ranasinghe, V. G. Zakrzewski, J. Gao, N. Rega, G. Zheng, W. Liang, M. Hada, M. Ehara, K. Toyota, R. Fukuda, J. Hasegawa, M. Ishida, T. Nakajima, Y. Honda, O. Kitao, H. Nakai, T. Vreven, K. Throssell, J. A. Montgomery, Jr., J. E. Peralta, F. Ogliaro, M. J. Bearpark, J. J. Heyd, E. N. Brothers, K. N. Kudin, V. N. Staroverov, T. A. Keith, R. Kobayashi, J. Normand, K. Raghavachari, A. P. Rendell, J. C. Burant, S. S. Iyengar, J. Tomasi, M. Cossi, J. M. Millam, M. Klene, C. Adamo, R. Cammi, J. W. Ochterski, R. L. Martin, K. Morokuma, O. Farkas, J. B. Foresman, D. J. Fox, Gaussian 16, Revision C.01, Gaussian, Inc., Wallingford CT, **2019**.

[26] S. Stoll, A. Schweiger, *J. Magn. Reson.* **2006**, *178*, 42–55.